

Check for updates



www.chemcatchem.org

# Efficient Synthesis of Porphyrin–Iridium Complex for Enhanced Cocatalyst-Free Photocatalytic Hydrogen Evolution

Govardhana Babu Bodedla,\*<sup>[a, b]</sup> Muhammad Imran,<sup>[c]</sup> Jianzhang Zhao,<sup>[c]</sup> Xunjin Zhu,\*<sup>[a, b]</sup> and Wai-Yeung Wong\*<sup>[a, b]</sup>

A new porphyrin–iridium complex, T-Ir-ZnPF, is synthesized facilely through a one-pot, nucleophilic substitution reaction between the iridium (Ir) complex Ir-NH<sub>2</sub> and zinc(II)-tetrakis(pentafluorophenyl)porphyrin ZnPF. In this porphyrin, the Ir-motif acts as a triplet energy donor, while the porphyrin moiety serves as a singlet energy acceptor. An efficient Förster resonance energy transfer from the Ir-motif to the porphyrin moiety enables exceptional light-harvesting capabilities in the broad ultraviolet–visible region, a longer photoexcited state electron lifetime, and a higher photoluminescent quantum yield for T-Ir-ZnPF compared to ZnPF without the Ir-motif. Moreover, T-Ir-ZnPF exhibits inhibition of aggregation-caused quenching,

resulting in suppressed nonradiative decay channels and consequently long-lived photoexcited states. The cocatalyst-free homogeneous photocatalytic hydrogen evolution (PHE) system of T-Ir-ZnPF produces a PHE rate ( $\eta H_2$ ) of 5.34 mmol g<sup>-1</sup> h<sup>-1</sup>. Under the same photocatalytic conditions, ZnPF did not produce hydrogen, while Ir-NH<sub>2</sub> delivered a very low  $\eta H_2$  of 0.20 mmol g<sup>-1</sup> h<sup>-1</sup>. Since the Stern–Volmer quenching constant of T-Ir-ZnPF is higher than those of ZnPF and Ir-NH<sub>2</sub>, the photoexcited reduced T-Ir-ZnPF species are formed more readily by gaining electrons from triethylamine. Subsequently, a direct and fast electron transfer from the reduced T-Ir-ZnPF to protons leads to a high cocatalyst-free PHE.

### 1. Introduction

Developing photocatalytic hydrogen evolution (PHE) systems has received much interest for producing sustainable green energy and reducing global warming issues arising from fossil fuel utilization. A typical PHE system is composed of a photosensitizer (PS), a sacrificial donor, and a cocatalyst. <sup>[1-4]</sup> To enhance the performance of the PHE system, the PS plays a major role among the components used in the PHE system. Thus, designing and synthesizing PSs have received much attention in recent years. So far, a range of PSs including inorganic composites, <sup>[3-6]</sup> graphitic carbon nitride (g-C<sub>3</sub>N<sub>4</sub>)-based

[a] Dr. G. B. Bodedla, Prof. X. Zhu, Prof. W.-Y. Wong Department of Applied Biology & Chemical Technology and Research Institute for Smart Energy, The Hong Kong Polytechnic University, Hong Kong, P. R. China

E-mail: govardhana.bodedla@polyu.edu.hk xunjin.zhu@polyu.edu.hk wai-yeung.wong@polyu.edu.hk

- [b] Dr. G. B. Bodedla, Prof. X. Zhu, Prof. W.-Y. Wong The Hong Kong Polytechnic University Shenzhen Research Institute, Shenzhen 518057, P. R. China
- [c] Dr. M. Imran, Prof. J. Zhao School of Chemical Engineering and State Key Laboratory of Fine Chemicals, Dalian University of Technology, Dalian 116024, P. R. China
- Supporting information for this article is available on the WWW under https://doi.org/10.1002/cctc.202500950
- © 2025 The Author(s). ChemCatChem published by Wiley-VCH GmbH. This is an open access article under the terms of the Creative Commons Attribution-NonCommercial-NoDerivs License, which permits use and distribution in any medium, provided the original work is properly cited, the use is non-commercial and no modifications or adaptations are made.

materials,<sup>[7–9]</sup> porous materials,<sup>[10–13]</sup> metal-complexes,<sup>[14–16]</sup> polymers, [17,18] carbon-based photocatalysts, [19] organic small molecules, [20–22] phthalocyanines, [4,23,24] and porphyrins [1,2,25,26] have been tested for PHE. Among the PSs, porphyrin-based materials endowed great focus in PHE due to their high lightharvesting ability in the broad ultraviolet-visible (UV-vis) region, stable electronic states for efficient photoinduced charge separation, and high photostability for long-term PHE.[27-29] Besides, the absorption, emission, and redox properties, as well as the separation and transport of photogenerated hole-electron pairs at the interface of the porphyrins can certainly be altered by conjugating several chromophores at the *meso*- and  $\beta$ -positions of porphyrin macrocycle and inclusion of various metals such as noble-metals and non-noble metals inside the porphyrin ring, thus achieving tunable PHE properties.[25,26,30,31] However, most of the porphyrin-based PHE systems require a cocatalyst, such as platinum (Pt) nanoparticles and Co-based complexes, to reduce the protons to molecular hydrogen (H<sub>2</sub>). This is mainly due to the lack of efficient photoinduced charge separation of photoexcited porphyrin and fast charge recombination, thereby prohibiting direct electron transfer from the photoexcited states of porphyrin to the proton. Hence, developing porphyrin-based PHE systems without a cocatalyst is an attractive goal for practical PHE technologies.

In this process, several groups, including ours, have developed cocatalyst-free PHE systems. [23,25,32-39] Recently, we have developed a mono-coordinated iridium (Ir)-motif conjugated porphyrin ZnP-T-Ir with a triazole linker for cocatalyst-free PHE. [40] Although this porphyrin possesses efficient Förster resonance energy transfer (FRET) for cocatalyst-free PHE, the synthesis of such a porphyrin involves many challenges, including low product yields and limited photostability. Contrarily, mono-

thed from https://chemistry-europe.onlinelibrary.wiley.com/doi/10.1002/cetc.202500950 by HONG KONG POLYTECHNIC UNIVERSITY HU NG HOM, Wiley Online Library on [29/09/2025]. See the Terms and Conditions (https://onlinelibrary.wiley.com/ems

and-conditions) on Wiley Online Library for rules of use; OA articles are governed by the applicable Creative Commons

Scheme 1. Synthetic route of T-Ir-ZnPF.

and tetra-coordinated Ir-motif conjugated porphyrins MBPyZnP-Ir and TBPyZnP-Ir, respectively, containing a bipyridyl linker did not produce any H<sub>2</sub> under cocatalyst-free conditions. This could be attributed to the large steric strain between the Irmotifs and the porphyrin ring in MBPyZnP-Ir and TBPyZnP-Ir which resulted in inefficient FRET from Ir-motif energy donor to porphyrin ring energy acceptor.<sup>[41]</sup> Likewise, the synthesis of MBPyZnP-Ir and TBPyZnP-Ir porphyrins is also very challenging due to the involvement of many synthetic steps with low product yields. These examples illustrate that molecular-engineered Ir-motif conjugated porphyrins play an important role in achieving cocatalyst-free PHE. Thus, we hypothesized that developing an easily synthesizable Ir-motif-based conjugated porphyrin with efficient FRET and high photostability would be an effective strategy for producing highly efficient cocatalyst-free PHE.

By considering the above points, herein, we synthesized a tetra-coordinated Ir-motif conjugated porphyrin T-Ir-ZnPF by a simple nucleophilic substitution reaction with a high yield (Scheme 1). The photophysical, electrochemical, transient absorption (TA), and PHE properties of T-Ir-ZnPF were studied and compared to those of ZnPF without Ir-motif and Ir-NH2 containing no porphyrin unit. Moreover, we also employed density functional theory (DFT) studies to get more insight into the optoelectronic properties and photoinduced charge separation of T-Ir-ZnPF and ZnPF. The results show that T-Ir-ZnPF delivered a PHE rate ( $\eta H_2$ ) of 5.34 mmol g<sup>-1</sup> h<sup>-1</sup>, which is much higher than that of the precursor Ir-NH<sub>2</sub> (0.20 mmol g<sup>-1</sup> h<sup>-1</sup>), under the same photocatalytic conditions, while ZnPF did not produce H<sub>2</sub>. The higher PHE performance of T-Ir-ZnPF than the Ir-NH<sub>2</sub> and ZnPF could be attributed to the high light harvesting ability, efficient photoinduced charge separation and long-lived photoexcited states. This subsequently triggered the direct electron transfer from photoexcited T-Ir-ZnPF to protons, resulting in H<sub>2</sub> production.

# 2. Results and Discussion

#### 2.1. Synthesis and Characterization of T-Ir-ZnPF

The tetra-coordinated Ir-motif conjugated porphyrin T-Ir-ZnPF was synthesized by a nucleophilic substitution reaction between the porphyrin ZnPF and the Ir-complex Ir-NH<sub>2</sub> under basic conditions in dimethylformamide (DMF) solvent (Scheme 1). The structure of T-Ir-ZnPF was characterized by nuclear magnetic resonance (NMR), matrix-assisted laser desorption ionization time-of-flight mass spectrometry (MALDI-TOF) and electrospray ionization-mass spectrometry (ESI-MS). T-Ir-ZnPF is soluble in acetone, acetonitrile, and tetrahydrofuran (THF), and is sparingly soluble in dichloromethane and DMF. The synthesis of ZnPF and Ir-NH<sub>2</sub> are shown in Schemes S1 and S2.

# 2.2. Photophysical, Electrochemical, and DFT Studies

Figure 1a shows the absorption spectra of ZnPF, Ir-NH<sub>2</sub>, and T-Ir-ZnPF recorded in the THF/water (H<sub>2</sub>O) (1:1, v/v) solvent mixture, and the corresponding data are presented in Table 1. Typically, Ir-NH<sub>2</sub> shows absorption from 220 to 500 nm, which contains two types of absorption peaks. The absorption peaks from 220 to 300 nm with a high molar extinction coefficient ( $\varepsilon$ ) belong to spin-allowed ligand-centered transitions ( $^{1}$ LC, i.e.,  $\pi-\pi^*$  transitions of C N ligands and N N ligands), whilst the peaks located at ca. 300 to 400 nm are related to the mixed transitions of singlet inter-ligand charge-transfer ( $^{1}$ LLCT) and singlet metal-to-ligand charge-transfer ( $^{1}$ MLCT). The absorption peaks with low  $\varepsilon$  observed in the lower energy region (ca. 550 nm) are attributed to the triplet transitions such as  $^{3}$ MLCT, as evident by time-dependent DFT (TDDFT) calculations. Two types of absorption bands in the region of 416–600 nm are observed for the

saded from https://chemistry-europe.onlinelibrary.wiley.com/doi/10.1002/cac.202500990 by HONG KONG POLYTECHNIC UNIVERSITY HU NG HOM, Wiley Online Library on [29/09/2025]. See the Terms and Conditions (https://onlinelibrary.wiley.com/erms

and-conditions) on Wiley Online Library for rules of use; OA articles are governed by the applicable Creative Commons I

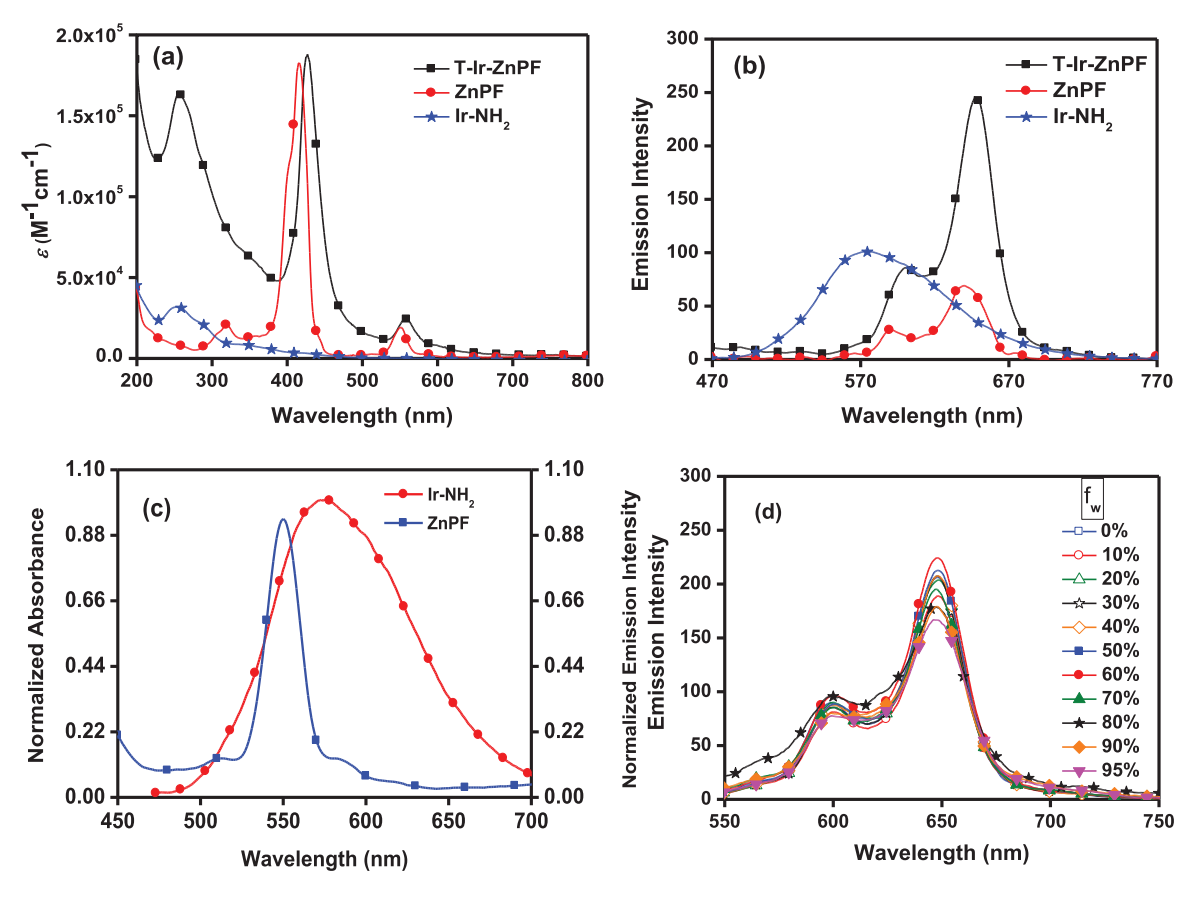


Figure 1. (a) Absorption and (b) emission spectra of T-Ir-ZnPF, Ir-NH<sub>2</sub>, and ZnPF recorded in THF/H<sub>2</sub>O (1:1; v/v, and 10  $\mu$ M) at room temperature under an argon atmosphere. (c) Overlapped absorption spectrum of ZnPF and emission spectrum of Ir-NH<sub>2</sub>. (d) Emission spectrum of T-Ir-ZnPF recorded in different ratio of  $f_w$  from 0% to 95% in the THF/H<sub>2</sub>O mixture (10  $\mu$ M). Note:  $\lambda_{ex}=410$  nm for ZnPF and  $\lambda_{ex}=360$  nm for T-Ir-ZnPF and Ir-NH<sub>2</sub>.

compound, ZnPF. The intensified absorption peak at 416 nm and weak absorption peaks in the range of 550-600 nm correspond to the Soret- and Q-bands, respectively, of the porphyrin macrocycle. Remarkably, the T-Ir-ZnPF shows a very broad absorption profile from 200 to 800 nm having mainly three types of absorption peaks. The intensified absorption peaks situated in the higher energy region (at ca. 220 to 350 nm) correspond to the Ir-motif absorption and the remaining two types of absorption peaks located at 426 and 550-606 nm belong to Soret- and Qbands of the porphyrin moiety, respectively. Moreover, the Soretand Q-bands of T-Ir-ZnPF are broadened and red-shifted by 10 nm compared to those of ZnPF, indicating the elongated conjugation resulting from the coupling of Ir-NH<sub>2</sub> and ZnPF. This trend is also well matched to the theoretically calculated absorption peak wavelengths of T-Ir-ZnPF and ZnPF (Table 2). Additionally, the experimentally measured absorption profile of T-Ir-ZnPF is well aligned with the theoretically simulated absorption profile (Figure S1). Notably, the intensity of absorption peaks belonging to Ir-motif in T-Ir-ZnPF is fourfold higher than those of Ir-NH<sub>2</sub>, attributed to the increased chromophore density which further confirms the presence of four Ir-motifs in T-Ir-ZnPF. All these results point out that conjugation of Ir-motif to porphyrin improves the light-harvesting property of porphyrin molecules in the entire UV-vis region and thus can act as a potential PS for PHE application. Nevertheless, the absorption peak positions of the Soret- and Q-bands did not change by increasing the  $H_2O$  fraction ( $f_w$ ) in the THF/ $H_2O$  mixture (Figure S2). It indicates the lack of aggregation ability of T-Ir-ZnPF in the THF/ $H_2O$  mixture and thus the homogeneous nature of T-Ir-ZnPF in the THF/ $H_2O$  mixture. This is much more beneficial to avoid charge recombination reactions of T-Ir-ZnPF during proton reduction under homogeneous PHE conditions ( $vide\ infra$ ). [34]

Figure 1b shows the emission spectra of the compounds recorded in the THF/H<sub>2</sub>O (1:1, v/v) solvent mixture, and the corresponding data are presented in Table 1. Ir-NH2 exhibits a broad emission peak with  $\lambda_{\text{em}}$  of 574 nm, which stems from the  $^3\text{MLCT}$ transition, whilst two porphyrins T-Ir-ZnPF and ZnPF show two emission peaks in the region of 590-650 nm which correspond to the porphyrin macrocycle. Moreover, a twofold increased emission intensity with a 10 nm red-shift in the T-Ir-ZnP emission peaks was noticed when compared to that of ZnPF without the Ir-motif. More specifically, in the emission profile of T-Ir-ZnPF, the emission peak at 574 nm assigned to Ir-motif has disappeared and only porphyrin emission peaks have appeared. This could be explained by the FRET from the Ir-motif to the porphyrin ring in T-Ir-ZnPF which depleted the Ir-motif peak intensity and gave rise to the enhanced porphyrin emission peak intensity. This result is also well consistent with the intensified emission peaks of T-Ir-ZnPF than ZnPF. As the emission peak at 574 nm due to Ir-motif completely disappeared and only the



| Table 1. Phot      | Table 1. Photophysical and electrochemical data of T-Ir-ZnPF, Ir-NH <sub>2</sub> , and ZnPF. |                          |                                |                                  |   |   |                                  |                           |                                     |  |  |  |  |
|--------------------|--|--------------------------|--------------------------------|----------------------------------|---|---|----------------------------------|---------------------------|-------------------------------------|--|--|--|--|
| Compound           | $\lambda_{\rm abs}^{\rm a)}(\varepsilon/10^4,  {\rm M}^{-1}  {\rm cm}^{-1})$ (nm)            | $\lambda_{em}^{a)}$ , nm | $\tau_{PL}^{\mathbf{b})}$ , ns | $\Phi_{\text{PL}}{}^{\text{c)}}$ | $E_{\mathrm{Ox}}$ d), eV ( $\Delta E_{\mathrm{p}}$ , mV)                    | $E_{\rm Red}^{ m e)}$ , eV ( $\Delta E_{ m p}$ , mV)                                    | $E_{(P}^{+}/_{P}^{*})^{f)}$ (eV) | $E_{(P}^*/P^-)^{g)}$ (eV) | E <sub>0-0</sub> <sup>h)</sup> (eV) |  |  |  |  |
| Ir-NH <sub>2</sub> | 253 (3.19), 286 (2.15), 351 (0.78), 425 (0.38)   | 574                      | 2100.0                         | 0.25                             | 1.62 (68) <sup>i)</sup>   | -1.07 (42) <sup>j)</sup> ,<br>- 1.84 (98) <sup>i)</sup>                                 | - 0.98                           | 1.53                      | 2.60                                |  |  |  |  |
| T-Ir-ZnPF          | 255 (16.38), 345 (6.47),<br>426 (18.80), 558 (2.47),<br>606 (0.74)                           | 600, 647                 | 14.0                           | 0.18                             | 1.64 (74) <sup>i)</sup> , 2.12 (60) <sup>j)</sup>                           | - 0.69 (95) <sup>i)</sup> ,<br>- 1.17 (74) <sup>i)</sup> ,<br>- 1.40 (44) <sup>j)</sup> | - 0.52                           | 1.47                      | 2.16                                |  |  |  |  |
| ZnPF               | 416 (18.1), 551 (1.96), 591 (0.27)   | 590, 639                 | 2.1                            | 0.12                             | 1.28 (50) <sup>j)</sup> , 1.58 (79) <sup>i)</sup> , 1.82 (91) <sup>i)</sup> | - 0.66 (73) <sup>i)</sup> ,<br>- 1.04 (58) <sup>j)</sup>                                | - 0.94                           | 1.56                      | 2.22                                |  |  |  |  |

 $<sup>^{\</sup>text{a})}$  THF/H $_2\text{O}$  (1:1; v/v, 10  $\mu\text{M})$  solution.

| Table 2. Calculated electronic transition properties of the low-lying electronic excited states of T-Ir-ZnPF and ZnPF based on B3LYP/GENECP/LANL2DZ level. |         |                        |                              |                 |                                |                  |                 |  |  |  |  |
|--|---------|------------------------|------------------------------|-----------------|--------------------------------|------------------|-----------------|--|--|--|--|
| Porphyrin  | States  | Electronic Transition  | Energy <sup>a)</sup> [eV/nm] | f <sup>b)</sup> | Composition <sup>c)</sup>      | CI <sup>d)</sup> | D <sup>e)</sup> |  |  |  |  |
| T-Ir-ZnPF  | Singlet | $S_0 \rightarrow S_1$  | 2.26 / 546                   | 0.0360          | HOMO → LUMO                    | 0.53165          | 9.41            |  |  |  |  |
|  |         | $S_0 \rightarrow S_2$  | 2.67 / 463                   | 0.0266          | $HOMO-3 \rightarrow LUMO + 3$  | 0.49057          |                 |  |  |  |  |
|  |         | $S_0 \rightarrow S_3$  | 2.84 / 436                   | 0.2597          | $HOMO \to LUMO + \!\!\!\! 4$   | 0.44977          |                 |  |  |  |  |
|  |         | $S_0 \rightarrow S_4$  | 2.88 / 429                   | 0.2250          | $HOMO-5 \rightarrow LUMO +1$   | 0.48753          |                 |  |  |  |  |
|  |         | $S_0 \rightarrow S_5$  | 2.90 / 426                   | 0.5220          | $HOMO-4 \rightarrow LUMO +1$   | 0.41319          |                 |  |  |  |  |
|  |         | $S_0 \rightarrow S_6$  | 2.92 / 424                   | 0.3255          | $HOMO-4 \rightarrow LUMO + 1$  | 0.48403          |                 |  |  |  |  |
|  | Triplet | $S_0 \rightarrow T_1$  | 1.63 / 757                   | 0.0000          | $HOMO \to LUMO$                | 0.57498          |                 |  |  |  |  |
|  |         | $S_0 \rightarrow T_2$  | 1.64 / 755                   | 0.0000          | $HOMO \to LUMO + \!\! 1$       | 0.56820          |                 |  |  |  |  |
|  |         | $S_0 \rightarrow T_3$  | 1.94 / 636                   | 0.0000          | $HOMO-1 \rightarrow LUMO$      | 0.61074          |                 |  |  |  |  |
|  |         | $S_0 \rightarrow T_4$  | 1.95 / 635                   | 0.0000          | $HOMO-1 \rightarrow LUMO + 1$  | 0.61823          |                 |  |  |  |  |
|  |         | $S_0 \rightarrow T_5$  | 2.45 / 505                   | 0.0000          | HOMO-10 $ ightarrow$ LUMO $+9$ | 0.27570          |                 |  |  |  |  |
| ZnPF   | Singlet | $S_0 \rightarrow S_1$  | 2.29 / 540                   | 0.0034          | $HOMO \rightarrow LUMO +1$     | 0.51900          | 0.00            |  |  |  |  |
|  |         | $S_0 \rightarrow S_2$  | 3.12 / 397                   | 1.5811          | $HOMO-1 \rightarrow LUMO +1$   | 0.41131          |                 |  |  |  |  |
|  |         | $S_0 \rightarrow S_3$  | 3.58 / 345                   | 0.0531          | $HOMO	ext{-2} 	o LUMO$         | 0.67259          |                 |  |  |  |  |
|  |         | $S_0 \rightarrow S_4$  | 3.73 / 331                   | 0.0092          | $HOMO-13 \rightarrow LUMO$     | 0.60928          |                 |  |  |  |  |
|  | Triplet | $S_0 \rightarrow T_1$  | 1.65 / 749                   | 0.0000          | $HOMO \to LUMO$                | 0.59951          |                 |  |  |  |  |
|  |         | $S_0 \rightarrow T_2$  | 1.95 / 635                   | 0.0000          | $HOMO-1 \rightarrow LUMO$      | 0.60211          |                 |  |  |  |  |
|  |         | $S_0 \rightarrow T_3$  | 3.03 / 408                   | 0.0000          | $HOMO-3 \rightarrow LUMO$      | 0.42272          |                 |  |  |  |  |
|  |         | $S_0 { ightarrow} T_4$ | 3.15 / 392                   | 0.0000          | $HOMO-4 \rightarrow LUMO$      | 0.44030          |                 |  |  |  |  |
|  |         | $S_0 \rightarrow T_5$  | 3.20 / 386                   | 0.0000          | HOMO → LUMO +2                 | 0.58109          |                 |  |  |  |  |

<sup>&</sup>lt;sup>a)</sup> Only the selected low-lying excited states are presented.

b) Calculated from emission lifetime decay spectra.

 $<sup>^{\</sup>rm Cl}$  TPP used as standard ( $\Phi_{PL}=0.85$  in THF) for ZnPF and T-Ir-ZnPF and [Ru(bpy)<sub>3</sub>]Cl<sub>2</sub> in degassed acetonitrile used as a reference ( $\lambda_{ex}=436$  nm with  $\Phi_{PL} =$  0.042) for Ir-NH<sub>2</sub>.

 $<sup>^{\</sup>rm d)}$   $E_{\rm ox}$  (vs. NHE) = 0.77 +  $E_{\rm ox}$  (vs. Ferrocene).

<sup>&</sup>lt;sup>e)</sup>  $E_{\text{red}}$  (vs. NHE) = 0.77 –  $E_{\text{red}}$  (vs. Ferrocene).

 $<sup>\</sup>begin{array}{l} f) \ E_{(P}{}^{+}/p^{*}) \ (\text{vs. NHE}) = E_{\text{Ox}} - E_{\text{0-0}}; \ \text{here "P" refers to PS.} \\ g^{0} \ E_{(P}{}^{*}/p^{-}) \ (\text{vs. NHE}) = E_{\text{Red}} + E_{\text{0-0}}; \ \text{here "P" refers to PS.} \\ \end{array}$ 

<sup>&</sup>lt;sup>h)</sup> Estimated from the intersection of the normalized absorption and emission spectra.

 $<sup>^{</sup>jj}$  Reversible wave. Note: The cyclic voltammograms of the compounds were recorded at a scan rate of 100 mV s<sup>-1</sup>.

b) Oscillator strengths.

c) Only the main configurations are presented.

d) The CI coefficients are in absolute values.

e) Ground state dipole moment values.



emission peaks at 600 and 647 nm corresponding to the porphyrin ring appeared in the emission spectra of T-Ir-ZnPF, we presume that the FRET from Ir-motif energy donor to the porphyrin ring energy acceptor has completely occurred in T-Ir-ZnPF porphyrin complex (Figure 1c). It should be noted that though FRET between the Ir-motif and the porphyrin ring has already been proven in tetra-coordinated Ir-motif conjugated porphyrin TBPyZnP-Ir, it did not completely occur due to the steric strain between the Ir-motif and the porphyrin ring in TBPyZnP-Ir, as observed by the emission peaks corresponding to the Ir-motif along with the porphyrin emission peaks in the emission profile of TBPyZnP-Ir. It indicates that the molecular design of T-Ir-ZnPF is much better than TBPyZnP-Ir for achieving complete FRET. The photoluminescence electron lifetime ( $\tau_{PL}$ ) of T-Ir-ZnPF, ZnPF and Ir-NH<sub>2</sub> was calculated to be 14.0, 2.1, and 2100.0 ns, respectively (Figure S3). Ir-NH<sub>2</sub> exhibited  $\tau_{PL}$  in the  $\mu$ s regime, indicating the triplet excited states involved in the emission while Ir-motif conjugated porphyrin T-Ir-ZnPF and ZnPF without Ir-motif showed the  $\tau_{PL}$  in the ns range, denoting that the singlet excited states contributed to the emission.

The excited state nature of the compounds was also studied by recording the emission spectra in the presence and absence of air (Figure S4). The emission intensity of Ir-NH<sub>2</sub> is reduced in the presence of air compared to that under argon, whereas the emission intensity of ZnPF and T-Ir-ZnPF remains the same in the presence of air and argon indicating the involvement of singlet excited states for both porphyrins. This result indicates that under photoexcitation, the FRET involves the triplet-to-singlet energy transfer from the Ir-motif to the porphyrin core in T-Ir-ZnPF. A similar type of Förster-type tripletto-singlet energy transfer is observed in the porphyrin-iridium complex ZnP-T-Ir.[40] This complex contains an Ir-motif that acts as a triplet energy donor and a porphyrin ring that serves as a singlet energy acceptor. These components are connected through a phenylene linkage, which plays a crucial role in facilitating energy transfer by providing a pathway for electronic communication between the donor and the acceptor. Similarly, the -NH linkage in T-Ir-ZnPF aids in enabling energy transfer between the donor and acceptor through electronic communication. Notably, a similar phenomenon has been observed in a decoupled donor-acceptor-based dyad, which includes an Irmotif as the triplet energy donor and a pyrene ring as the singlet energy acceptor.<sup>[42]</sup> In the decoupled dyad system, the spatial arrangement and electronic properties of the donor and acceptor are optimized to enhance the efficiency of the energy transfer process. More notably, the emission intensity of T-Ir-ZnPF was not quenched upon increasing the H<sub>2</sub>O fraction in the THF/H<sub>2</sub>O solvent mixture (Figure 1d). It indicates that T-Ir-ZnP inhibited the aggregation-caused quenching (ACQ) phenomenon, which is beneficial for suppressing nonradiative deactivating channels and thus provides long-lived photoexcited states.[30] Additionally, instead of FRET, the possibility of electron transfer between Ir-motif and porphyrin ring in T-Ir-ZnPF was further studied by recording the emission spectra of T-Ir-ZnPF in nonpolar and polar solvents. As seen in Figure S5, the emission wavelength of T-Ir-ZnPF does not vary with increasing solvent polarity. It indicates that the excited state electron transfer between Ir-motif and porphyrin ring is not possible in T-Ir-ZnPE.[43]

To investigate the FRET from the Ir-motif to the porphyrin center, we conducted a TA study of the excited-state dynamics at the nanosecond (ns) timescale for the photoexcited T-Ir-ZnPF (Figure 2). We observed strong apparent ground state bleaching (GSB) bands at the wavelengths of 420 and 670 nm (Figure 2a). The band at 670 nm was attributed to stimulated emission (SE), consistent with the steady-state emission spectra. However, this SE band vanished at longer delay times. To extract the individual components of these observations, we employed global fitting analysis on the raw data, resulting in evolution-associated difference spectra (EADS) as shown in Figure 2b. The first component, with a lifetime of ca. 17.4 ns, exhibited two GSB bands at both 420 and 670 nm, which aligns with the  $\tau_{PL}$  depicted in Figure S3(a). This component at early delay times is ascribed to the S<sub>1</sub> state. Subsequently, the component featured a longer delay time which lacked 670 nm GSB band while persisting with the 420 nm GSB, and additionally displayed positive absorption bands in the range of 360-540 nm. Therefore, we attributed the first component to the S<sub>1</sub> state and the second one to the T<sub>1</sub> state, justifying the FRET from the Ir-motif to the porphyrin moiety in T-Ir-ZnPF.

Excited-state oxidation  $(E_{(P}^+/_P^*)$  and reduction  $(E_{(P}^*/_P^-))$ potential values of PSs always play a decisive role in estimating the plausibility of electron transfer from photoexcited states of PS to proton and in receiving an electron from a sacrificial donor in photoexcited states of PS during the PHE mechanism.[33,44] However, for the calculation of such potential values, firstly the redox potentials, such as the first oxidation potential  $(E_{Ox})$  and reduction ( $E_{Red}$ ) potential values of PSs, need to be calculated by performing the cyclic voltammetric experiments (Figure S6). The calculated  $E_{Ox}$  values of Ir-NH<sub>2</sub>, ZnPF, and T-Ir-ZnPF are 1.62, 1.28, and 1.68 eV, respectively, while the values -1.07, -0.66, and -0.69 eV correspond to the  $E_{Red}$  of Ir-NH<sub>2</sub>, ZnPF, and T-Ir-ZnP, respectively. Secondly,  $E_{(P}^{+}_{/P}^{*})$  and  $E_{(P}^{*}_{/P}^{-})$  values were calculated from  $E_{ox}$  and  $E_{Red}$  using Rehm-Weller equations (see footnote of Table 1). Accordingly, the  $E_{(P}^{+}/_{P}^{*})$  values of Ir-NH<sub>2</sub>, ZnPF, and T-Ir-ZnPF were calculated to be -0.98, -0.94, and -0.52 eV, respectively, and the  $E_{(P}^*/P^-)$  values of Ir-NH<sub>2</sub>, ZnPF, and T-Ir-ZnPF were calculated to be 1.53, 1.56, and 1.47 eV, respectively. For better understanding, the energy level alignments of photocatalytic components such as PSs and sacrificial donor are shown in Figure 3a. It was found that for three PSs the  $E_{(P}^{+}/P^{*})$  values are higher-lying than the H<sup>+</sup>/H<sub>2</sub> and  $E_{(P}^{*}/P^{-})$  values are lower-lying than the sacrificial donor triethylamine (TEA) redox potential. This indicates the transfer of electrons from photoexcited PSs to protons directly for proton reduction and the transfer of electrons from TEA to reduced PSs for regenerating PSs are thermodynamically favorable processes.

The ground state-optimized geometries of T-Ir-ZnPF and ZnPF are presented in Figure 3b. For both porphyrins, the twist angles of the fluorinated aryl rings with the porphyrin core lie in the range of 68.5°–73.6°, which is typical for *meso*-tetraarylporphyrins. For T-Ir-ZnPF, as the two units are connected via an amino flexible linker, the dihedral angles between Irmotifs and fluorinated aryl rings are in the range of 135.0°–138.0°. For T-Ir-ZnPF, the excitation energy of the singlet excited states

sed from https://chemistry-europe.on/inelibrary.wiley.com/doi/10.1002/cctc.202500950 by HONG KONG POLYTECHNIC UNIVERSITY HUNG HOM, Wiley Online Library on [29/09/2025]. See the Terms and Conditions (https://onlinelibrary.wiley.com/erms

and-conditions) on Wiley Online Library for rules of use; OA articles are governed by the applicable Creative Commons I

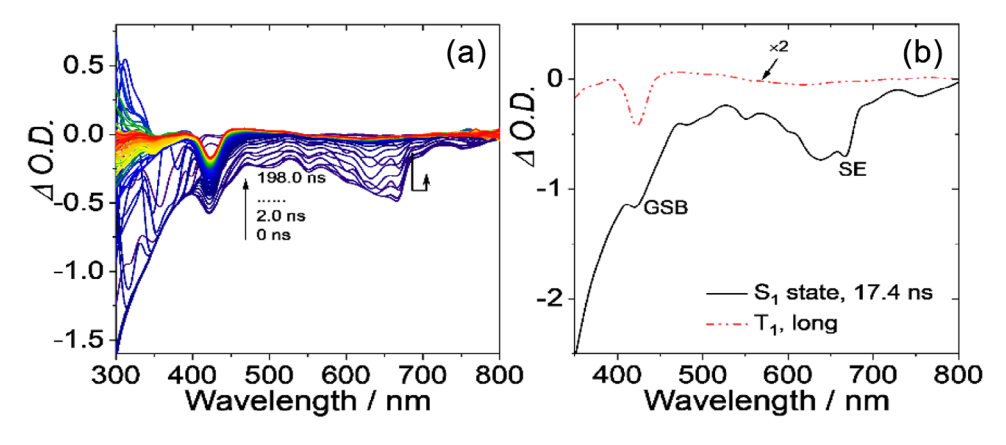


Figure 2. (a) ns-TA spectra of T-Ir-ZnPF in deaerated THF/ $H_2$ O (1:1; v/v, and 10  $\mu$ M) in a short delay time range upon pulsed laser excited at 355 nm and 25 °C. (b) Evolution-associated difference spectra of the ns-TA spectra obtained after global analysis.

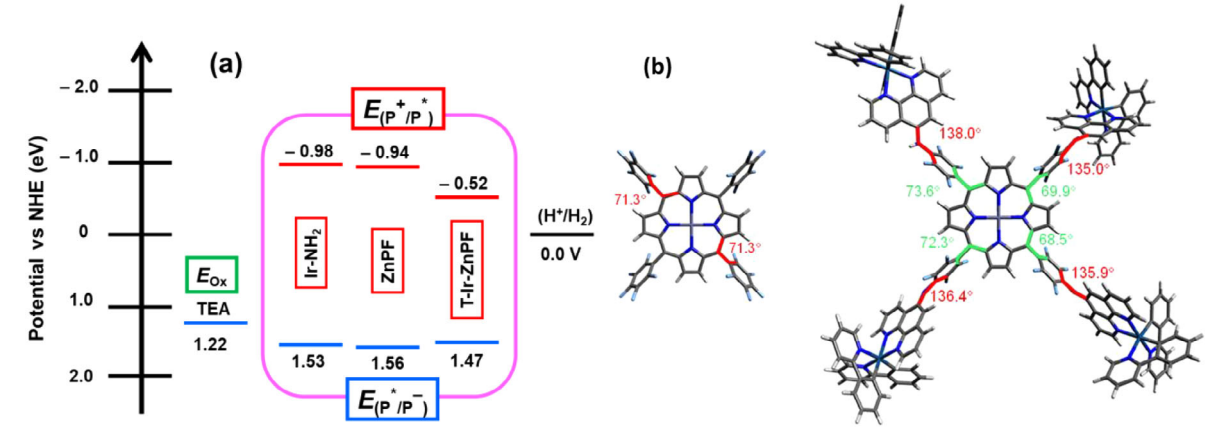


Figure 3. (a) Energy level alignments of the components used in the photocatalytic systems. (b) Optimized geometries of ZnPF (left) and T-Ir-ZnPF (right).

was calculated with the TDDFT method (Figure S8 and Table 2). Two low-lying isoenergetic singlet excited states (S<sub>1</sub> and S<sub>2</sub> states) were obtained, which are confined to the two Ir-motifs. The S<sub>1</sub> state is a charge transfer state, involving a highest occupied molecular orbital (HOMO) to lowest unoccupied molecular orbital (LUMO) transition, while the higher singlet excited state  $(S_n \text{ state})$  is confined to the porphyrin unit. The calculated excitation energy is in good agreement with the UV-vis absorption experimental results (vide supra). The triplet state energy levels of T-Ir-ZnPF were calculated with the TDDFT method based on the optimized ground state geometry. Two close-lying degenerated triplet states were obtained (T<sub>1</sub> and T<sub>2</sub> states), which are localized on the two Ir-motifs. The frontier molecular orbitals of the T-Ir-ZnPF complex and controlled ZnPF are shown in Figure 4 and Figure S7. For T-Ir-ZnPF, the HOMO is exclusively localized on the Ir moieties, and the LUMO is mainly localized on the porphyrin unit and slightly extended to the linker parts. This result indicates that charge transfer is possible from the Ir-motifs to the porphyrin unit in T-Ir-ZnPF under photoexcitation.[26,33]

Moreover, the spatial separation of the HOMO and LUMO in T-Ir-ZnPF leads to the generation of efficient charge-separated excited states upon photoexcitation. Thus, efficient photoin-duced charge (hole-electron pair) separation and migration of photogenerated carriers in T-Ir-ZnPF are expected when it is

used as a PS in PHE application. Contrarily, the contribution of both the HOMO and LUMO on the porphyrin unit in ZnPF suggests the lack of photoinduced charge separation ability. Theoretically calculated ground state dipole moment (approximated from the optimized ground state geometry by DFT calculations) values of T-Ir-ZnPF and ZnPF are 9.41 and 0.00 D, respectively. The higher dipole moment value of T-Ir-ZnPF compared to ZnPF further supports that the separation of the photogenerated hole-electron pair and migration of electrons are greater for T-Ir-ZnPF.[38,45] The calculated electrostatic potential (ESP) maps are further used to predict the donor-acceptor interactive behavior of the molecules (Figure S7). In T-Ir-ZnPF, consistent with the HOMO/LUMOs, ESP analysis showed that the Ir-motif carries a negative charge and serves as an electron donor while the blue electron-deficient region on the central porphyrin is an electron acceptor.

#### 2.3. PHE Studies

The cocatalyst-free PHE performance of Ir-NH<sub>2</sub>, ZnPF, and T-Ir-ZnPF was evaluated by employing them as PSs in photocatalytic systems containing a TEA sacrificial donor and THF/H<sub>2</sub>O mixture (1:1 v/v) as the proton source. As shown in Figure 5a,

doi/10.1002/ccc.20250050 by HONG KONG POLYTECHNIC UNIVERSITY HUNG HOM, Wiley Online Library on [29/09/2025]. See the Terms and Conditions (https://onlinelibrary

and-conditions) on Wiley Online Library for rules of use; OA articles are governed by the applicable Creative Commons

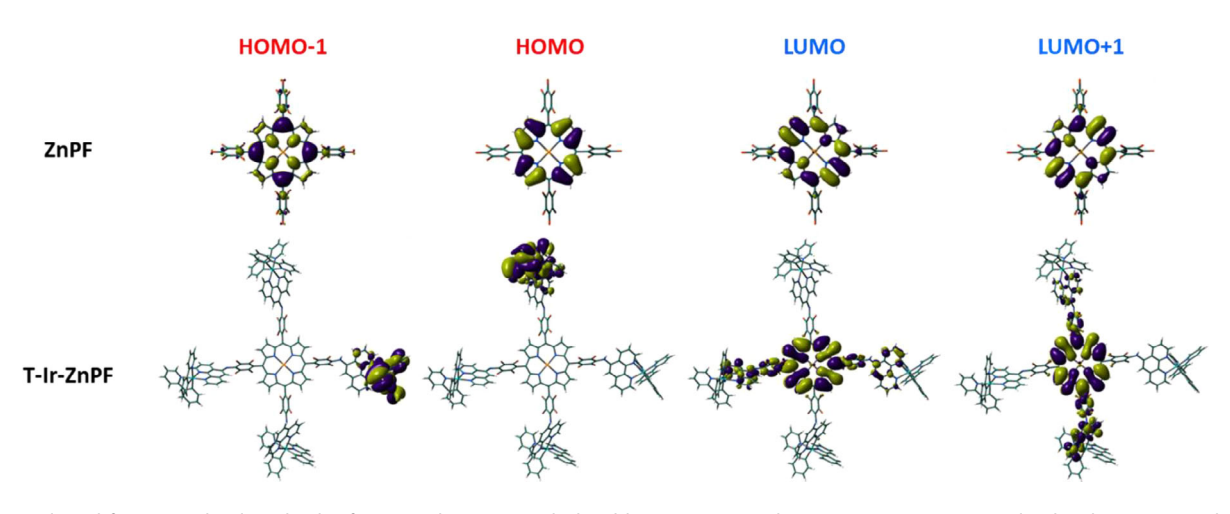


Figure 4. Selected frontier molecular orbitals of ZnPF and T-Ir-ZnPF calculated by using DFT at the B3LYP/GENECP/LANL2DZ level with Gaussian 16 based on the optimized ground-state geometries. Isovalue = 0.01.

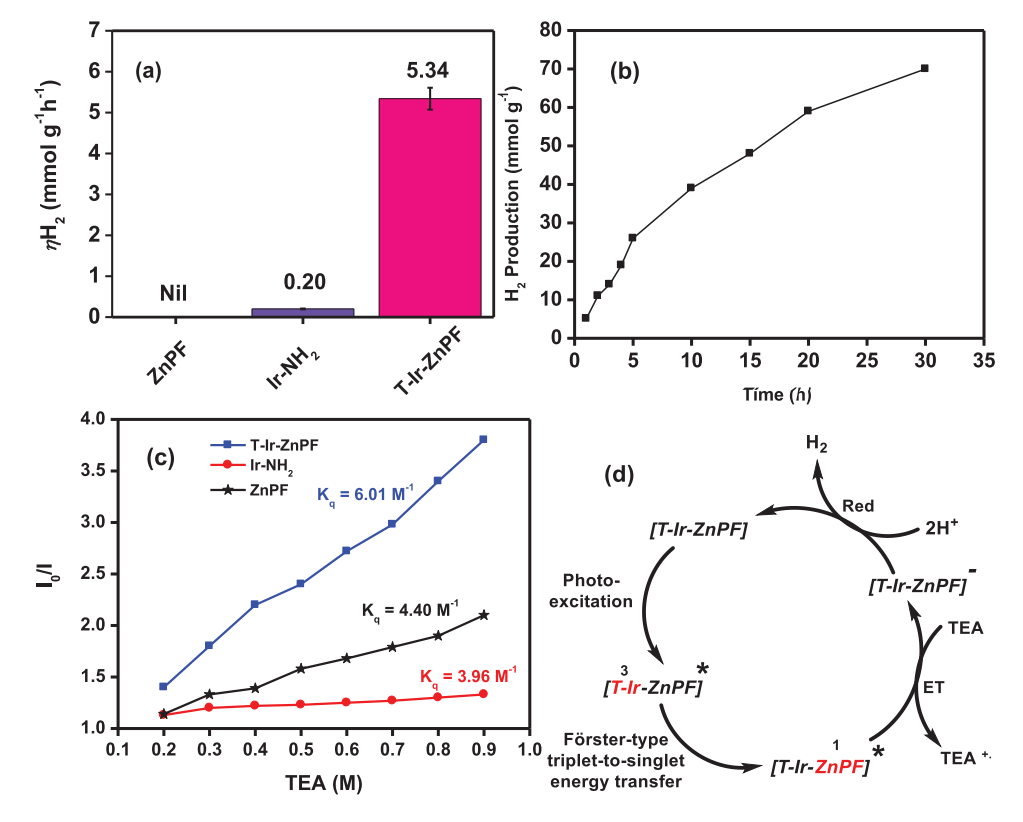


Figure 5. (a)  $\eta H_2$  of photocatalytic systems of Ir-NH<sub>2</sub>, ZnPF, and T-Ir-ZnPF under irradiation for 5 h: Ir-NH<sub>2</sub>/ZnPF/T-Ir-ZnPF (10 μM), TEA (0.8 M), and THF/H<sub>2</sub>O (1:1, v/v). (b) H<sub>2</sub> production of photocatalytic system of T-Ir-ZnPF under irradiation for 30 h: T-Ir-ZnPF (10 μM), TEA (0.8 M), and THF/H<sub>2</sub>O (1:1, v/v). (c) Stern–Volmer plot of T-Ir-ZnPF, Ir-NH<sub>2</sub>, and ZnPF in THF/H<sub>2</sub>O (1:1, v/v) with TEA as a quencher. (d) Plausible PHE mechanism of T-Ir-ZnPF. ET is electron transfer. and Red is reduction.

T-Ir-ZnPF produced a very high  $\eta H_2$  of 5.34 mmol  $g^{-1}$  h<sup>-1</sup> compared to that of Ir-NH<sub>2</sub> (0.20 mmol  $g^{-1}$  h<sup>-1</sup>). However, ZnPF did not produce any H<sub>2</sub>. The higher  $\eta H_2$  of T-Ir-ZnPF compared to Ir-NH<sub>2</sub> and ZnPF could be ascribed to the following factors: (i) high light-harvesting property in the UV-vis region, (ii) enhanced photoexcited  $\tau_{PL}$  due to FRET between Ir-motif and porphyrin ring, (ii) ACQ inhibition which restricts the charge recombination, and (iv) suitable HOMO and LUMO energy levels and high dipole moment value for efficient photoinduced

charge separation. More significantly, under the same cocatalyst-free PHE conditions, the previously reported mono-coordinated Ir-motif conjugated porphyrin ZnP-T-Ir and heteroleptic Ir(III) complex Ir-2 containing trifluoromethyl groups delivered  $\eta H_2$  of 0.42 and 0.8 mmol g<sup>-1</sup> h<sup>-1</sup>, respectively, which are much lower than that of T-Ir-ZnPF (Figure S9). [133,40] Contrarily, the tetra-coordinated Ir-motif conjugated porphyrin TBPyZnP-Ir did not produce any  $H_2$ . [41] It indicates that the molecular design of T-Ir-ZnPF is very effective for producing efficient cocatalyst-

Chemistry Europe

European Chemical Societies Publishing

free PHE. Notably, the cocatalyst-free PHE performance of T-Ir-ZnPF significantly surpasses that of the previously reported efficient photocatalysts.[35,46-53] To further understand the role of cocatalyst on the PHE performance of T-Ir-ZnPF, the  $\eta H_2$  of T-Ir-ZnPF was evaluated in the presence of cocatalysts such as chloro(pyridine)cobaloxime (CoPyCI) and Pt nanoparticles (Figure S10). T-Ir-ZnPF exhibited  $\eta H_2$  of 6.20 and 7.40 mmol g<sup>-1</sup> h<sup>-1</sup> in the presence of CoPyCl and Pt cocatalysts, respectively. It demonstrates that the addition of cocatalysts did not improve the PHE performance of T-Ir-ZnPF. This result reveals that T-Ir-ZnPF has less charge (hole-electron pair) recombination reactions and thus a direct electron transfer from photoexcited porphyrin moiety of T-Ir-ZnPF to proton for H<sub>2</sub> production without the use of a cocatalyst. Moreover, the PHE of T-Ir-ZnPF increased continuously from the initial time of light irradiation to 30 h, indicating the photostability of T-Ir-ZnPF (Figure 5b). Also, the UV-vis absorption profile of T-Ir-ZnPF did not change before and after 30 h of light irradiation, which also attests to the photostability of T-Ir-ZnPF (Figure S11).

Since the optimization of photocatalytic conditions plays a major role in producing efficient PHE, we further screened all plausible conditions for the T-Ir-ZnPF photocatalytic system. Initially, we performed the PHE test of T-Ir-ZnPF without the addition of TEA in the photocatalytic system. However, H2 was not detected from the photocatalytic system of T-Ir-ZnPF. This indicates that TEA is needed to produce active T-Ir-ZnPF species for PHE. Then, we varied the ratio of the THF and H<sub>2</sub>O mixture of the photocatalytic system and the results show that the use of 1:1, v/v of THF/H<sub>2</sub>O mixture is the best condition for realizing the maximum  $\eta H_2$  (Figure S12(a)). Later on, the TEA concentration effect was also tested. Increasing the concentration of TEA from 0.1 to 0.5 M increased the  $\eta H_2$  of T-Ir-ZnPF, but a concentration higher than 0.8 M TEA led to a lower PHE performance (Figure S12(b)). The substitution of TEA with triethanolamine (TEOA), ethylenediaminetetraacetic acid (EDTA), and ascorbic acid (AA) did not improve the  $\eta H_2$  of the T-Ir-ZnPF photocatalytic system (Figure S13). All these results emphasize that the photocatalytic system containing 10  $\mu M$  of T-Ir-ZnPF and 0.8 M of TEA in a 1:1, v/v of THF/H2O mixture is the best-optimized condition for highly efficient cocatalyst-free PHE.

To propose the PHE mechanism involved in the photocatalytic systems, we performed the photoluminescence quenching experiments of PSs with the sacrificial donor TEA. As shown in Figure S14, the photoluminescence of all PSs was progressively quenched with a rising concentration of TEA. This implies that the electron transfer from TEA to PSs is viable.[39] The order of calculated Stern-Volmer quenching constant ( $K_{\alpha}$ ) of PSs with the TEA quencher is as follows: T-Ir-ZnPF (6.01 M<sup>-1</sup>) > ZnPF (4.40  $M^{-1}$ ) > Ir-NH $_2$  (3.96  $M^{-1}$ ) (Figure 5c). Since the  $K_q$  of T-Ir-ZnPF is higher than those of ZnPF and Ir-NH<sub>2</sub>, the photoexcited reduced T-Ir-ZnPF species are formed more readily by receiving electrons from TEA. Subsequently, a direct and fast electron transfer from the reduced T-Ir-ZnPF to protons leads to high H<sub>2</sub> production. Based on the PHE results and photoluminescence quenching studies, a reductive quenching mechanism can be proposed to the T-Ir-ZnPF during PHE mechanism. The detailed PHE mechanism of T-Ir-ZnPF is shown in Figure 5d.

#### 3. Conclusion

In summary, a new tetra-coordinated Ir-motif conjugated porphyrin, T-Ir-ZnPF, was synthesized and characterized through absorption, emission, redox, and PHE studies. DFT calculations were performed to gain more insight into the optoelectronic and photoinduced charge transfer properties of the porphyrins. Absorption, emission, and TA studies indicate that T-Ir-ZnPF possesses complete triplet-to-singlet FRET between the Ir-motif and porphyrin ring due to the overlapping emission peak of the Ir-motif and the Q-band absorption peak of the porphyrin ring. This results in an enhanced light-harvesting ability, long-lived photoexcited states, and consequently a longer photo excited  $\tau_{PL}$  for T-Ir-ZnPF compared to ZnPF. Furthermore, T-Ir-ZnPF possesses suitable HOMO and LUMO energy levels and a higher dipole moment value than ZnPF, leading to efficient photoinduced charge separation in the porphyrin. Photoluminescence quenching experiments suggest that the photoexcited reduced T-Ir-ZnPF species form more readily than those of Ir-NH<sub>2</sub> and ZnPF due to the high-lying  $E_{(P}^*/P^-)$  value. As a result of these beneficial properties, T-Ir-ZnPF exhibited higher cocatalyst-free PHE performance than ZnPF and Ir-NH2. Additionally, the cocatalyst-free PHE performance of T-Ir-ZnPF was comparable to that observed in the presence of a cocatalyst. Notably, T-Ir-ZnPF not only exhibited higher cocatalyst-free PHE performance than our previously reported mono-coordinated Ir-motif conjugated porphyrin ZnP-T-Ir but was also highly photostable.

#### **Acknowledgments**

G.B.B acknowledges the financial support from the Start-up Fund for Research Assistant Professors (RAPs) under the Strategic Hiring Scheme (P0048725) of the Hong Kong Polytechnic University. W.-Y.W. acknowledges the financial support from the RGC Senior Research Fellowship Scheme (SRFS2021-5S01), the National Natural Science Foundation of China (52073242), the Hong Kong Polytechnic University (YXA2), Research Institute for Smart Energy (CDAQ), Research Centre for Nanoscience and Nanotechnology (CE2H), Research Centre for Carbon-Strategic Catalysis (CE2L and CE01), and Miss Clarea Au for the Endowed Professorship in Energy (847S). The research was also supported by the grants (HKBU 12304320 and N\_HKBU213/22) from the Hong Kong Research Grants Council.

# **Conflict of Interests**

The authors declare no conflicts of interest.

# **Data Availability Statement**

The data that support the findings of this study are available from the corresponding author upon reasonable request.

**Keywords:** Cocatalyst-free · Iridium-motif · Photocatalytic hydrogen evolution · Porphyrin · Triplet-to-singlet FRET

- J. S. O'Neill, L. Kearney, M. P. Brandon, M. T. Pryce, Coord. Chem. Rev. 2022, 467, 214599.
- [2] M. Joseph, S. Haridas, Int. J. Hydrog. Energy 2020, 45, 11954–11975.
- [3] X. Zhang, T. Peng, S. Song, J. Mater. Chem. A 2016, 4, 2365–2402.
- [4] G. B. Bodedla, X. Zhu, W.-Y. Wong, EnergyChem 2024, 6, 100138.
- [5] X. Hao, Y. Shao, D. Xiang, Z. Jin, Sol. Energy Mater. Sol. Cells 2022, 248, 111070
- [6] X. Zheng, Y. Song, Y. Liu, Y. Yang, D. Wu, Y. Yang, S. Feng, J. Li, W. Liu, Y. Shen, X. Tian, Coord. Chem. Rev. 2023, 475, 214898.
- [7] L. Chen, X. Liang, H. Wang, Q. Xiao, X. Qiu, Chem. Eng. J. 2022, 442, 136115
- [8] S. Wan, J. Xu, S. Cao, J. Yu, Interd. Mater. 2022, 1, 294–308.
- [9] L. Li, G. B. Bodedla, Z. Liu, X. Zhu, Appl. Surf. Sci. 2020, 499, 143755.
- [10] Z. Lian, Z. Li, F. Wu, Y. Zhong, Y. Liu, W. Wang, J. Zi, W. Yang, Commun. Chem. 2022, 5, 93.
- [11] X. Li, Q. Dong, Q. Tian, A. Sial, H. Wang, H. Wen, B. Pan, K. Zhang, J. Qin, C. Wang, *Mater. Today Chem.* 2022, 26, 101037.
- [12] Y. Li, X. Song, G. Zhang, L. Wang, Y. Liu, W. Chen, L. Chen, ChemSusChem 2022, 15, e202200901.
- [13] S. Ghosh, A. Nakada, M. A. Springer, T. Kawaguchi, K. Suzuki, H. Kaji, I. Baburin, A. Kuc, T. Heine, H. Suzuki, R. Abe, S. Seki, J. Am. Chem. Soc. 2020, 142, 9752–9762.
- [14] D. N. Tritton, F.-K. Tang, G. B. Bodedla, F.-W. Lee, C.-S. Kwan, K. C.-F. Leung, X. Zhu, W.-Y. Wong, Coord. Chem. Rev. 2022, 459, 214390.
- [15] S. Chen, Y. Wang, Y. Huang, Y. Zhang, P. Deng, ACS Sustainable Chem. Eng. 2023, 11, 2704–2712.
- [16] S. Guo, K.-K. Chen, R. Dong, Z.-M. Zhang, J. Zhao, T.-B. Lu, ACS Catal. 2018, 8, 8659–8670.
- [17] G. Zhang, Z.-A. Lan, X. Wang, Angew. Chem., Int. Ed. 2016, 55, 15712–15727.
- [18] Y. Bai, Z. Hu, J.-X. Jiang, F. Huang, *Chem. Asian J.* **2020**, *15*, 1780–1790.
- [19] Z. Li, K. Li, P. Du, M. Mehmandoust, F. Karimi, N. Erk, Chemosphere 2022, 308, 135998.
- [20] A. Dolan, J. M. de la Perrelle, T. D. Small, E. R. Milsom, G. F. Metha, X. Pan, M. R. Andersson, D. M. Huang, T. W. Kee, ACS Appl. Nano Mater. 2022, 5, 12154–12164.
- [21] X. Yuan, C. Wang, L. Vallan, A. T. Bui, G. Jonusauskas, N. D. McClenaghan, C. Grazon, S. Lacomme, C. Brochon, H. Remita, G. Hadziioannou, E. Cloutet, Adv. Funct. Mater. 2023, 33, 2211730.
- [22] G.-Y. Wang, S. Guo, P. Wang, Z.-M. Zhang, T.-B. Lu, *Appl. Catal. B: Environ*.
- [23] A. C. Yüzer, E. Genc, G. Kurtay, G. Yanalak, E. Aslan, E. Harputlu, K. Ocakoglu, I. Hatay Patir, M. Ince, Chem. Comm. 2021, 57, 9196–9199.
- [24] S. Keshipour, A. Asghari, *Int. J. Hydrog. Energy* **2022**, *47*, 12865–12881.
- [25] G. B. Bodedla, Y. Dong, G. Tang, J. Zhao, F. Zhang, X. Zhu, W.-Y. Wong, J. Mater. Chem. A 2022, 10, 13402–13409.
- [26] G. B. Bodedla, V. Piradi, M. Imran, J. Zhao, X. Zhu, W.-Y. Wong, J. Mater. Chem. A 2023, 11, 1473–1481.
- [27] G. B. Bodedla, J. Huang, W.-Y. Wong, X. Zhu, ACS Appl. Nano Mater. 2020, 3, 7040–7046.
- [28] G. B. Bodedla, G. Tang, J. Zhao, X. Zhu, Sustainable Energy Fuels 2020, 4, 2675–2679.
- [29] G. B. Bodedla, L. Li, Y. Che, Y. Jiang, J. Huang, J. Zhao, X. Zhu, Chem. Comm. 2018, 54, 11614–11617.

- [30] G. B. Bodedla, X. Zhu, W.-Y. Wong, Aggregate 2023, 4, e330.
- [31] G. B. Bodedla, X. Zhu, Z. Zhou, W.-Y. Wong, Top. Curr. Chem. 2022, 380, 49.
- [32] C. Zhang, H. Pan, C. Chen, Y. Zhou, ACS Macro Lett. 2022, 11, 434-440.
- [33] G. B. Bodedla, D. N. Tritton, X. Chen, J. Zhao, Z. Guo, K. C.-F. Leung, W.-Y. Wong, X. Zhu, ACS Appl. Energy Mater. 2021, 4, 3945–3951.
- [34] Y. Ji, Q. Zuo, C. Chen, Y. Liu, Y. Mai, Y. Zhou, Chem. Comm. 2021, 57, 4174–4177.
- [35] D. Huo, F. Lin, S. Chen, Y. Ni, R. Wang, H. Chen, L. Duan, Y. Ji, A. Zhou, L. Tong, *Inorg. Chem.* 2020, 59, 2379–2386.
- [36] L. Liu, S. Du, X. Guo, Y. Xiao, Z. Yin, N. Yang, Y. Bao, X. Zhu, S. Jin, Z. Feng, F. Zhang, J. Am. Chem. Soc. 2022, 144, 2747–2754.
- [37] G.-L. Zhang, T.-Y. Yang, J. Zhang, Y.-H. Zhang, ChemCatChem 2023, 15, e202201271.
- [38] Z. Zhang, Y. Zhu, X. Chen, H. Zhang, J. Wang, Adv. Mater. 2019, 31, 1806626.
- [39] G. B. Bodedla, V. Piradi, W. Thor, K.-L. Wong, X. Zhu, W.-Y. Wong, J. Mater. Chem. A 2024, 12, 2924–2931.
- [40] K. Zheng, G. B. Bodedla, Y. Hou, J. Zhang, R. Liang, J. Zhao, D. Lee Phillips, X. Zhu, J. Mater. Chem. A 2022, 10, 4440–4445.
- [41] D. N. Tritton, G. B. Bodedla, G. Tang, J. Zhao, C.-S. Kwan, K. C.-F. Leung, W.-Y. Wong, X. Zhu, J. Mater. Chem. A 2020, 8, 3005–3010.
- [42] A. Cravcenco, M. Hertzog, C. Ye, M. N. Iqbal, U. Mueller, L. Eriksson, K. Börjesson, Sci. Adv. 2019, 5, eaaw5978.
- [43] J. Kandhadi, W.-C. Yan, F. Cheng, H. Wang, H.-Y. Liu, New J. Chem. 2018, 42, 9987–9999.
- [44] G. B. Bodedla, W.-Y. Wong, X. Zhu, J. Mater. Chem. A 2021, 9, 20645– 20652
- [45] H. Lin, J. Wang, J. Zhao, Y. Zhuang, B. Liu, Y. Zhu, H. Jia, K. Wu, J. Shen, X. Fu, X. Zhang, J. Long, *Angew. Chem., Int. Ed.* 2022, *61*, e202117645.
- [46] H. Szalad, A. Uscategui-Linares, R. García-Muelas, A. Galushchinskiy, O. Savateev, M. Antonietti, J. Albero, H. García, ACS Appl. Mater. Interfaces 2024, 16, 67597–67608.
- [47] Y. Jiang, C.Y. Toe, S.S. Mofarah, C. Cazorla, S.L.Y. Chang, Y. Yin, Q. Zhang, S. Lim, Y. Yao, R. Tian, Y. Wang, T. Zaman, H. Arandiyan, G.G. Andersson, J. Scott, P. Koshy, D. Wang, C.C. Sorrell, ACS Sustainable Chem. Eng. 2023, 11, 3370–3389.
- [48] C. Imparato, G. Iervolino, M. Fantauzzi, C. Koral, W. Macyk, M. Kobielusz, G. D'Errico, I. Rea, R. Di Girolamo, L. De Stefano, A. Andreone, V. Vaiano, A. Rossi, A. Aronne, RSC Adv. 2010, 10, 12519–12534.
- [49] X. Shi, L. Mao, P. Yang, H. Zheng, M. Fujitsuka, J. Zhang, T. Majima, Appl. Catal. B: Environ. 2020, 265, 118616.
- [50] W. Lei, H. Wang, S. Khan, N. Suzuki, K. Takagi, K.-i. Katsumata, K. Teshima, C. Terashima, A. Fujishima, J. Colloid Interface Sci. 2023, 645, 219–226.
- [51] M. Song, Y. Wu, G. Zheng, C. Du, Y. Su, Appl. Surf. Sci. 2019, 498, 143808.
- [52] H.N. Kim, T.W. Kim, I.Y. Kim, S.-J. Hwang, Adv. Funct. Mater. 2011, 21, 3111–3118.
- [53] N. Liu, J. Jiang, S. Zhang, R. Zhang, M. Xu, Z. Chen, P. Cheng, W. Shi, Angew. Chem., Int. Ed. 2025, e202501141, https://doi.org/10.1002/anie. 202501141.

Manuscript received: June 6, 2025 Accepted manuscript online: June 9, 2025 Version of record online: June 28, 2025